CrystEngComm

Accepted Manuscript

This article can be cited before page numbers have been issued, to do this please use: M. Hamad, C. Boissier, V. M. Calo, J. Gale, S. O. Nilsson Lill, G. Parkinson and A. Rohl, *CrystEngComm*, 2023, DOI: 10.1039/D2CE01426B.




ROYAL SOCIETY OF CHEMISTRY

rsc.li/crystengcomm

View Article Online
DOI: 10.1039/D2CE01426B

ARTICLE

# Quasi-static Deformation Simulations of Molecular Crystals

Mustafa S. Hamad,[a] Catherine Boissier,[b] Victor M. Calo,[c] Julian D. Gale,[a] Sten O. Nilsson Lill,[d] Gordon M. Parkinson,[e] Andrew L. Rohl,[f]*

Received 00th January 20xx,
Accepted 00th January 20xx

DOI: 10.1039/x0xx00000x

Identification of the mechanical performance of pharmaceuticals in the drug discovery process can determine the tabletability of a target molecule. Determination of the active slip systems and their ranking in molecular crystals is challenging because molecules offer a set of configurational variables absent from metallic or simple ionic materials, such as bond rotations, molecular rotations, and the relative orientation of molecules. This paper uses two computational methods, the rigid-block and tensor-based shearing methods, to calculate the slip barriers and gain insights regarding the slip deformation of simple molecular crystalline materials, using diatomic solid oxygen and anthracene as examples. Both methods use constrained quasi-static energy minimisation to simulate the materials' displacement and homogeneous shearing. These shearing methods rank the slip systems in oxygen and anthracene in agreement with experiment, including those reported herein where two previously unknown active slip systems in the basal plane of anthracene were identified independently from the computations. Internal degrees of freedom, in the form of shear-induced molecular rotations, critically influence the slip barriers and deformation mechanism. Our results uncover rotational twinning, which is linked to crystallographic symmetry rather than partial dislocations, while homogeneous shear of anthracene leads to a series of polymorphic transitions. The results also provide alternative interpretations of slip-observed morphologies.

## 1. Introduction

Knowledge of the mechanical performance of pharmaceutical crystals expedites the design and manufacture of medicinal tablets. Pharmaceutical crystals characterised by medium hardness correlate with good compaction performance[1]. This mechanical response of pharmaceuticals is related to the number of active slip systems in materials; for example, paracetamol form I only has two active slip systems leading to it having only limited deformability[2], and thus explains its difficult compaction. In principle, finding and sorting the active slip systems based on ease of slip in pharmaceuticals provides insights regarding their mechanical performance and tabletability.

Slip systems, characterised by crystallographic planes and directions, are essential to understanding the space of possible deformation. Hence, significant experimental work has sought to find the active slip systems in crystalline materials. Dislocation etch pit techniques[3,4] determine active slip systems using chemical processes. Slip line analysis[5], is another general method applicable to different classes of materials that can find the active slip system(s) but cannot rank them. This ranking requires specialised experiments such as micropillar compression at pre-set orientations[5, 6]. Electron beams are deleterious to organic molecular crystals; thus, only recently has the scanning electron microscope [7] been used to resolve the orientation map of an organic molecular crystal, a polycrystalline rubrene thin film. Despite such advances, the experimental determination of active slip systems remains challenging, being protracted and expensive; this provides the motivation to try to develop theoretical and computational procedures to find and rank these systems instead.

Elementary dislocation theory predicts that the Burgers vector (a geometric quantity describing dislocations) parallel to the shortest lattice vector should be the slip direction, and either the crystallographic plane of the largest interplanar spacing or a stacking fault plane coincides with the active slip plane [8]. Such insights have succeeded in FCC [9], BCC [10], HCP metals [11], ionic crystals [12], and some organic molecular crystals [13]. Kojima [13] suggested that predicted active slip systems in organic

a. Curtin Institute for Computation and School of Molecular and Life Sciences, Curtin University, P.O. Box U1987, Perth, WA 6845, Australia.
b. Oral Product Development, Pharmaceutical Technology & Development, Operations, AstraZeneca Gothenburg, SE-431 83, Mölndal, Sweden.
c. School of Electrical Engineering, Computing and Mathematical Sciences, Curtin University, P.O. Box U1987, Perth, WA 6845, Australia
d. Data Science & Modelling, Pharmaceutical Sciences, R&D, AstraZeneca Gothenburg, SE-431 83, Mölndal, Sweden.
e. Curtin University of Technology, Office of Research and Development, P. O. Box U1987, Perth, WA 6845, Australia.
f. Curtin Institute for Computation and School of Electrical Engineering, Computing and Mathematical Sciences, Curtin University, P.O. Box U1987, Perth, WA 6845, Australia. E-mail: andrew.rohl@curtin.edu.au

† Electronic Supplementary Information (ESI) available: Force field and cell representation of $\beta$-oxygen; Illustrations and details of tested slip systems of $\beta$-oxygen; ESP derived partial charges of anthracene; Convergence analysis for $\beta$-oxygen and anthracene; Slip movies of $\beta$-oxygen deformation; Finding the angle between crystallographic planes in a rhombohedral cell; Rotational twinning movies of $\beta$-oxygen; Characterisation of slip systems in anthracene by TEM; RBSM and TBSM molecular rotations in anthracene (001)[010]; RBSM rotational twinning in anthracene (001)[110]; RBSM rotational twinning in anthracene (001)[100]; Mechanically-induced polymorphic transitions in anthracene; Higher accuracy quantum mechanical methods; RMSD15 analysis of the virtual polymorphs. A selection of simulation input files have also been deposited with the ESI to assist in the reproducibility of our results. The files have the *.gin* extension and can be run using the General Utility Lattice Program (GULP).
`See DOI: 10.1039/x0xx00000x

View Article Online
DOI: 10.1039/D2CE01426B





molecular crystals conform to dislocation theory criteria. However, Gallagher *et al.* [14] used dislocation slip analysis on pentaerythritol tetranitrate (PETN) to find that the active slip system's direction is longer than the shortest Burgers vector. They attributed this finding to factors beyond dislocation theory, such as strong bond anisotropy and a complex molecular geometry whose lattice translation may result in unfavourable contact between molecules. Since the work of Gallagher *et al.*, several groups have used computational techniques to study defects and slip barriers in organic molecular crystals. The simplest method uses the attachment energy[15] (i.e., the energy released due to the growth of a surface layer on a growing crystal face[16]) to rank the slip systems. Sun and Kiang[16] analysed fourteen different organic crystals and found that the success rate for this approach is less than 50 %. Methods similar to the generalised stacking fault energy (GSFE)[17] have been used to estimate the slip barriers of anthracene by shearing one half of a crystal of rigid molecules with respect to another[18], predicting the (010)[001] to be the easiest slip system, which is inconsistent with the experimentally observed slip systems of (001)[010] and (001)[110][19] [20]. Munday *et al.*[21] proposed a variant of the GSFE method to calculate the energy barriers and evaluate slip versus cleavage of several slip systems in αRDX. Whereas two rigid blocks are only sheared relative to each other in the traditional GSFE method[17], the variant of Munday *et al.* improves the relaxation scheme. Thus, this modified approach can allow for some conformational states of molecules during energy minimisation. Nevertheless, this variant cannot resolve a large portion of the GSFE surface unless the fully-relaxed region size is relatively small[21] [22], which limits the conformational space being probed, thereby missing important configurations. Indeed, slip in molecular crystals can produce not only conformational changes but also polymorphic transitions, as shown for aspirin[23] and paracetamol[24]. Therefore, a fast and robust computational procedure that can rank the slip systems based on ease of slip and uncover conformational changes and phase transformations associated with such processes is of interest.

This paper addresses the problem of identifying and ranking the slip systems in molecular crystals. We study β-oxygen, an example of the simplest molecular system known (a homonuclear diatomic molecule), that has two equivalent axes of rotation and a close-packed (111) structure similar to FCC metals. Comparing the ranking of its slip systems with FCC metals will therefore provide insights regarding the interplay of molecular rotations and slip barriers. Anthracene is a planar molecular crystal and exhibits the next deformation complexity level after diatomic crystals, with three distinct rotational axes but no internal conformational degrees of freedom. Figure 1 shows the unit cells of β-oxygen and anthracene with additional molecules for completeness, in addition to the planes where

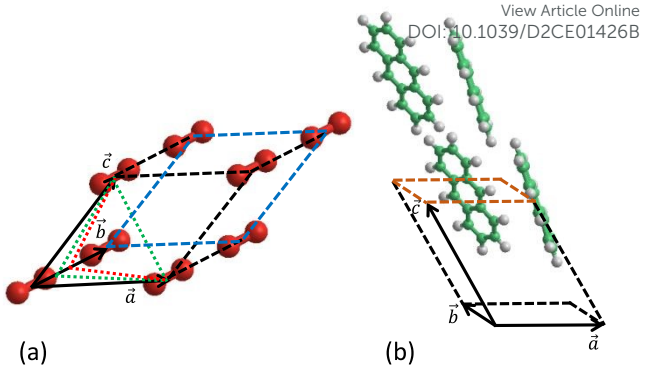


Figure 1: Illustrations of the unit cells of (a) oxygen and (b) anthracene, containing one and two molecules per cell, respectively (all other molecules shown are periodic images). For oxygen, the planes bound by the blue, red, and green dashed lines denote the annealed-induced twinning planes[25]; (010), (121), and (141). For anthracene, the plane bound by the brown dashed lines denotes the active slip plane.

twinning has been observed in β-oxygen [25] and the active slip plane in anthracene[19] [20]. We introduce two quasi-static computational methods, namely the Rigid-Block Shearing Method (RBSM) and Tensor-Based Shearing Method (TBSM), to simulate the athermal shearing of these two molecular systems along several slip directions. For every material, we summarise the map of the slip barriers across the attempted slip systems and highlight interesting deformation mechanisms, such as rotational twinning and phase transitions. Transmission electron microscopy (TEM) images of deformation-induced dislocations in anthracene have been used to identify two new active slip systems in the basal plane. Finally, we discuss the relevance of the estimated slip barriers and deformation mechanisms and compare them to other experimental observations.

## 2. Materials and Methods

This section provides background information about diatomic oxygen and anthracene, their crystal phases, details of the force field models used, and the slip systems to be tested. In addition, the last subsection describes the computational methods used to simulate shear deformation and extract slip barriers.

### Solid Oxygen

Oxygen has three polymorphs at low temperatures and pressures[26]. Here we focus on the $\beta$-oxygen polymorph, which adopts a rhombohedral crystal structure (space group $R\bar{3}m$) with one molecule per unit cell and the vector connecting every two oxygen atoms parallel to the [111] direction[27]. This results in a structure where the (111) plane is very similar to the (111) plane in FCC metals and these planes stack in an ABC motif. Kobashi *et al.*[27] reviewed several force fields to model the interactions in solid oxygen[28,29,30]. Their findings suggest that the force field developed by Cheung as reported by Powles and Gubbins[30] best reproduces the doubly-degenerate librational frequency in $\beta$-oxygen; hence we have chosen to adopt this force field. The supplementary material (section S1) details the force field and the hexagonal and rhombohedral cell representations we use, while noting that our reference system is

 

always the rhombohedral cell with lattice vector, *a*, of 4.07 Å and rhombohedral angle 48.3°.

Despite the limited stability range for the solid phase, surprisingly, there is experimental data on the active slip systems and the deformation mechanisms in $\beta$-oxygen. Venables *et al.*[25] reported experimentally observed annealing-induced twins not only of the stacking-fault type similar to FCC metals, but also of the rotational twinning type in higher index planes. This report motivates our study of the deformation in several crystallographic planes; (111), (110), (112), (113), (114), (115), and (116). For the (111) plane, we simulate deformation in the $[10\bar{1}]$ and $[11\bar{2}]$ directions, where the latter is the known twinning direction in FCC metals. We perform five deformation simulations for the remaining slip systems, each with the slip directions shown in Figure 2 to scan the principal directions. For deformation simulations in higher index directions, we use the intuitive annotated directions as per Figure 2(a), rather than the actual crystallographic directions. We choose the principal direction relative to the "twin" direction, which is the direction anti-parallel to the projection of the molecular vector onto a slip plane. For clarity, we show these directions by dashed arrows lying in the (110) and (112) planes in Figure 2(b). The "anti-twin" direction is anti-parallel to the "twin" one, while the "diagonal" direction is orthogonal to both directions and has a symmetry-equivalent direction at 180°. The "45°" and "135°" directions are at the specified angles with respect to the "twin" direction and have their symmetry-equivalent counterparts at -45° and -135°, respectively. We find the corresponding crystallographic directions using the Weiss Zone law[31] to determine the list of directions that match the "twin" direction. Then, based on their angles, we chose the relevant directions. Supplementary material section S2, Table S.2, provides the details of these directions with respect to the slip systems tested for oxygen, and Figures S2.1 to S2.7 illustrate them.

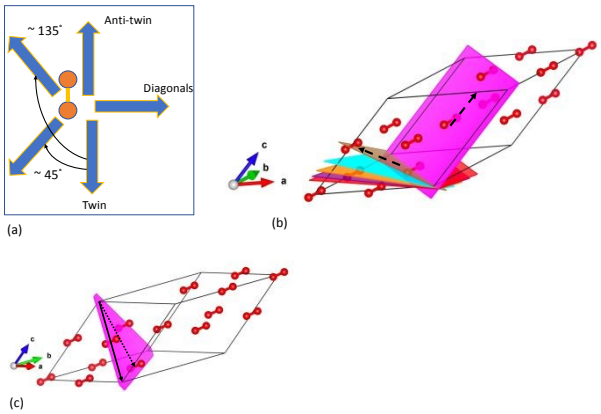


Figure 2: Schematic diagrams of (a) the notation referring to the slip directions to be simulated for $\beta$-oxygen in each plane except (111), (b) the rhombohedral cell of $\beta$-oxygen with slip planes (110), (112), (113), (114), (115), and (116) drawn in pink, brown, cyan, orange, purple, and red, respectively, and (c) the rhombohedral cell of $\beta$-oxygen with the (111) plane indicated in pink and the $[10\bar{1}]$ and $[11\bar{2}]$ directions indicated with the solid and dashed arrows, respectively. Visualisations in (b) and (c) were produced using the VESTA software [32].

Deformation simulations of diatomic oxygen involve molecule rotations. We quantify such angular distortions by defining the inclination angle, $\delta$, as the angle between the molecular vector and the *z*-axis, and the azimuth angle, $\theta$, as the angle between the projection of the molecular vector onto the *xy* plane and the *x*-axis, as shown in supplementary material, Figure S2.8; Table S2.1 reports the inclination angles prior to the deformation simulations.

**Anthracene**

Anthracene ($C_{14}H_{10}$) is a planar aromatic hydrocarbon composed of three benzene rings, characterised by photoplastic effects[13], and is proposed to have three polymorphs[33]. At standard temperature and pressure, anthracene crystallises in a monoclinic unit cell (space group P21/a) having two molecules per unit cell[34]. The General Amber Force Field (GAFF) [35] was employed to model the interactions in anthracene with a maximum cut-off of 10 Å. The electrostatic potential-derived partial charges of carbon and hydrogen atoms were computed using Gaussian [36] at the HF/6-311G(1d,1p) level of theory, see supplementary material, Figure S3.1. Table 1 shows the level of agreement between the calculated and experimental lattice parameters of anthracene. While there is a general underestimation of the cell lengths, partly due to the neglect of thermal and zero point effects, there is excellent agreement with the monoclinic angle. The calculated interplanar angle, $\kappa$, between the normal vectors to the molecular planes of anthracene molecules in the unit cell of 45° is in excellent agreement with a previous calculation[37] (44.5°), which used a different force field,[38] and relatively similar to experiment (≅ 55.5°).[37]

There exists ample experimental evidence that the active slip systems in anthracene are the (001)[110] and (001)[010][19] [20]. Our TEM imaging of deformed anthracene crystals finds two other active slip systems that we report later. Growth-induced twins were observed in the basal plane of anthracene,[39] which suggests the existence of 1/2 [110] partial dislocations that may help explain the origin of tilt boundaries [40]. Resel *et al.*[41] proposed the existence of a phase transition in anthracene due to the application of anisotropic pressure, confirmed via diffraction patterns. Recently, anisotropic compression molecular dynamics simulations[37] predicted a polymorphic transition and provided the lattice parameters and atomic coordinates. These simulations indicate mechanically-induced polymorphic transitions in anthracene associated with slip. We compute the slip barriers and demonstrate the plasticity of anthracene by simulating six main slip systems: (001)[010], (001)[110], (001)[100], (001)$[\bar{1}10]$, (001)$[\bar{1}00]$, and (001)$[\bar{1}20]$.

Table 1: Comparison of the optimised lattice parameters of anthracene obtained using the GAFF force field with those from experiment at 290 K (CSD identifier ANTCEN).

| Lattice Parameter | a (Å) | b (Å) | c (Å) | $\alpha$ ° | $\beta$ ° | $\gamma$ ° |
|---|---|---|---|---|---|---|
| GAFF | 8.257 | 5.929 | 10.914 | 90.00 | 124.48 | 90.00 |
| Experiment[34] | 8.562 | 6.038 | 11.184 | 90.00 | 124.42 | 90.00 |
| Error (%) | 3.6 | 1.8 | 2.2 | - | 0.0 | - |

As per the case of oxygen, we expect that angular rotations of anthracene molecules will be observed as a function of strain; thus, we define a basis set of vectors for every molecule, as per Figure 3, in addition to visualising the slip systems and molecular stacking. Let the basis set $\overrightarrow{e_p}$, where subscript $p$ represents the principal basis vectors, be arranged column-wise in a matrix form, $\boldsymbol{E}$, where $\boldsymbol{E_0}$ represents the basis in the reference configuration (energy-minimum configuration which coincides with the experimental configuration, see Table 1), and $\boldsymbol{E_f}$ the same for a deformed configuration, $f$. Let the rotation tensor, $\boldsymbol{T}$, represent a 3D rotation mapping in a right-handed orthonormal basis that can be decomposed into three basic rotations about the $x$, then $y$, and finally the $z$-axis, that is, $\boldsymbol{T} = T_{z(\alpha)}T_{y(\beta)}T_{x(\gamma)}$. We determine the Eulerian angles $\alpha$, $\beta$, and $\gamma$ by solving;

$$T = E_0 E_f^{-1} \quad (1)$$

for every deformed configuration, which determines the angular rotations of anthracene molecules as a function of strain.

## Methods

We employ two computational methods based on quasi-static energy minimisation procedures to simulate the shear deformation of crystalline materials. By applying external constraints on the system, we calculate the system's energy by minimising the other degrees of freedom for every strain step, thus providing the strain energy profile of the system. Systems subject to shear deformation

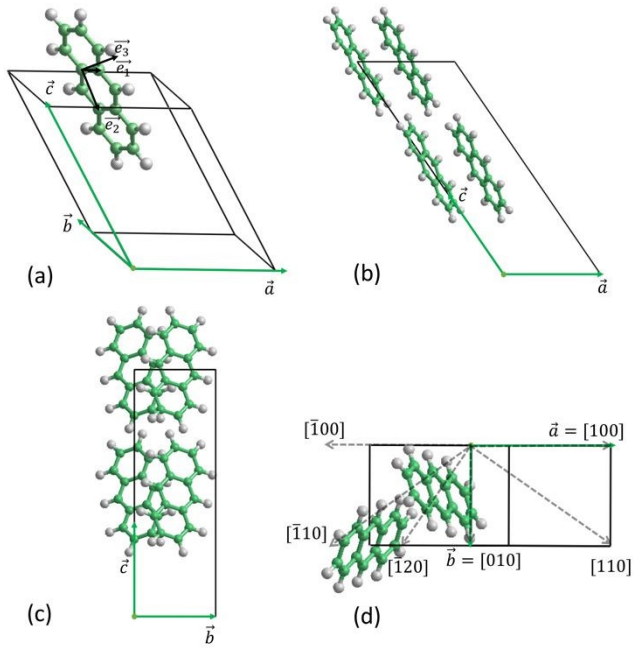


Figure 3: Schematic showing an anthracene molecule in its monoclinic unit cell in (a), while the second molecule per cell is hidden. The basis $\overrightarrow{e_1}$, $\overrightarrow{e_2}$, and $\overrightarrow{e_3}$ vectors are constructed as per the solid vectors in black, *i.e.* using the coordinates of the ring carbon atoms to produce $\overrightarrow{e_1}$, $\overrightarrow{e_2}$. (b) and (c) show the a-c and the b-c views of an anthracene supercell. (d) shows the top view ($z$-axis) of an anthracene unit cell with the slip directions drawn in dashed grey arrows.

in quasi-static, or even dynamic, simulations will ultimately hit an instability point, where one or more phonons become imaginary. Here we utilise the rational function optimisation (RFO) [42] method, which analyses the eigenvalues of the Hessian matrix to find these imaginary modes and remove them, thereby lowering the symmetry when appropriate and producing "slipped" configurations. Three crucial advantages come from using RFO: First, all the quasi-statically minimised configurations are physically stable, as all phonons are real, at least at the centre of the Brillouin zone. Second, no prior knowledge of the "slipped" configurations is required as RFO finds them whenever the system reaches the point of instability. Third, combining force fields with RFO in shear methods makes the calculations much faster than either higher accuracy quantum mechanical methods or large-scale molecular dynamics; thus, our methods are appropriate for the rapid scanning of many potential slip systems. The motivation behind the proposal of the two computational techniques is to simulate two different shear experiments, namely "simple" versus "pure" shearing[43] ( where the latter is also known as homogeneous, or affine shearing), ultimately enabling the comparison of the performance of these methods in finding slip barriers and deformation mechanisms. Below, we provide the technical details of these two computational methods.

**Method 1: Rigid Block Shearing Method (RBSM).** The RBSM method shears 2D periodic surface cells, which here are produced using GDIS.[44] Once a surface cell has been constructed, where the surface is the slip plane of interest, the user divides the simulation cell into three regions, where the atoms in regions 2 and 3 are fixed at the bulk structure (*i.e.,* the regions are rigid blocks) during the optimisation step and those in region 1, which lies between regions 2 and 3, are free to relax. Then the translation vector (slip direction) is specified in the plane of this surface and, as Figure 4 shows, impose shear by translating region 3 with respect to region 2 over a particular number of steps, leading to strain saturating region 1. For every shear step, the internal energy is minimised subject to the

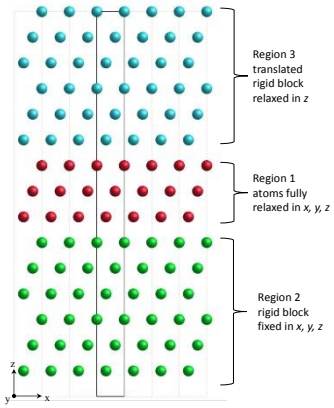


Figure 4: Schematic showing the configuration of a surface cell for RBSM. The system encompasses the molecules confined by the solid rectangle, with images shown in the x

View Article Online
DOI: 10.1039/D2CE01426B





direction to emphasise the periodic nature of the simulations. The constraints on each region are noted, while molecules are represented as spheres for simplicity.

constraint that region 3 cannot relax with respect to region 2 except in the direction orthogonal to translation. There are two important size parameters for RBSM-type calculations: First, the sizes of the two rigid blocks have to be sufficient to converge the interaction energies with region 1. Second, the number of layers in region 1 has to be varied to establish convergence for this parameter, which influences the extent of relaxation that can occur.

Here we define the dimensionless normalised strain energy, $U_N$, as;

$$U_N = \frac{\Delta U}{N_a E_c} \quad (2)$$

where $\Delta U$ is the difference in the potential energy (internal energy) between the strained and equilibrium surface cell, $N_a$ is the number of molecules in region 1, and $E_c$ is the bulk cohesive/lattice energy per molecule. The strain for the system is calculated according to;

$$\gamma_b = \frac{d_{R3}}{h} \quad (3)$$

where $\gamma_b$ is the Voigt shear strain, $d_{R3}$ is the shear displacement of region 3, and $h$ is the height in z of region 1. The combination of the shear strain and $U_N$ before slip is useful in finding the slip barrier of a trial slip system, as will be shown later.

RBSM is a "simple shear" deformation method that uses the displacement of rigid blocks to deform the bulk structure, whose formalism has been implemented in the General Utility Lattice Program (GULP) [45] and can readily be applied to a wide spectrum of materials given the availability of many different force fields. Analysis of the influence of shear step size and system size (of region 1) for oxygen and anthracene is given in the supplementary material section S4. Convergence of the curve up to the point of slip is achieved in oxygen and anthracene by having at least 12 and 10 layers in region 1, respectively, at a strain step equal to or less than 0.0008 and 0.008 strain/step, again respectively. Anthracene has partial charges and hence it is necessary to calculate its electrostatic interactions. This is achieved in GULP[45] by using Parry sum [46,47] which calculates electrostatic interactions for surface cells such as those used in RBSM.

**Method 2: Tensor-Based Shearing Method (TBSM).** TBSM applies homogeneous shear deformation to supercells, which are produced here using the General Purpose Trajectory Analyser (GPTA),[48] in a particular slip plane and along a specified slip direction. The homogeneous shear deformation of a supercell implies the homogeneous mapping of lattice vectors and atomic coordinates. For example, Figure 5 illustrates a two-dimensional shearing of a solid sphere model for simplicity. In the general case, TBSM deforms materials through an applied strain and, thus, optimises configurations at finite strain with respect to a reference configuration. Hence the lattice vectors for any state expressed as a 3x3 matrix, $\boldsymbol{R}$, are the product of the Voigt strain matrix, $\boldsymbol{\varepsilon}$, and the lattice vectors of the reference configuration, $\boldsymbol{R_0}$:

$$\boldsymbol{R} = \boldsymbol{\varepsilon R_0} \quad (4)$$

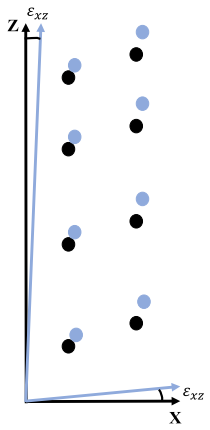


Figure 5: Schematic application of a strain tensor to a 2-D arbitrary solid-sphere model. Solid circles represent atoms in the system. The axes and atoms coloured in black are the reference configuration. Upon applying $\varepsilon_{xz}$ , i.e. $\varepsilon_5$ *in (5)*, the axes and atomic positions are deformed, and the new configuration is coloured in light blue.

For completeness, the Voigt strain matrix is:

$$\begin{pmatrix} 1+\varepsilon_1 & \frac{1}{2}\varepsilon_6 & \frac{1}{2}\varepsilon_5 \\ \frac{1}{2}\varepsilon_6 & 1+\varepsilon_2 & \frac{1}{2}\varepsilon_4 \\ \frac{1}{2}\varepsilon_5 & \frac{1}{2}\varepsilon_4 & 1+\varepsilon_3 \end{pmatrix} \quad (5)$$

TBSM fixes one or more components of the Voigt strain matrix and relaxes all other components. For instance, a material could be sheared by a total strain of 0.4 for one matrix component in 500 steps, where the configuration is quasi-statically minimised at every step, thus yielding the coordinate and lattice vector trajectories and energy profiles. The strain derivatives for a pairwise interaction between two atoms with vector, $v$, and length, $r$, in terms of the application of the strain matrix to the initial reference vector, $v_0$, are conveniently written in terms of the square of the distance as;

$$\left(\frac{\partial U}{\partial \varepsilon}\right) = \left(\frac{1}{r}\frac{\partial U}{\partial r}\right)\left(\frac{1}{2}\frac{\partial r^2}{\partial \varepsilon}\right) \quad (6)$$

where the distance squared is determined according to;

$$r^2 = v_0^T \varepsilon^T \varepsilon v_0 \quad (7)$$

Since the strain matrix is symmetric, its transpose is used only for formal correctness. This quadratic form is readily differentiated with respect to the strain. Instead of taking the limit of all strains to zero after differentiating and identifying the derivatives for each strain component, here we preserve the finite strain structure and compute the derivatives accordingly. The extension to the second derivatives with respect to strains for the Hessian matrix follows the same procedure.

DOI: 10.1039/D2CE01426B

As anthracene has partial charges on its atoms, it is necessary to use the Ewald summation[49,50] to obtain a well-converged electrostatic energy. Computing the finite strain derivatives for the real space contribution follows the above procedure, as per two-body potentials. However, the derivatives of both the reciprocal lattice vectors and cell volume are needed in reciprocal space. Both derivatives are related to the inverse of the strain matrix via the expression for the lattice vectors. Differentiating the inverse strain matrix uses the implicit function theorem leading to;

$$\left(\frac{\partial \varepsilon^{-1}}{\partial \zeta}\right) = -\varepsilon^{-1}\left(\frac{\partial \varepsilon}{\partial \zeta}\right)\varepsilon^{-1} \qquad (8)$$

where $\zeta$ is any degree of freedom (*i.e.*, any of the six strain components). The above formalism for working at finite strain with respect to a reference configuration has been implemented in GULP [45] for 1D, 2D, and 3D systems and the majority of available force fields. This formalism allows any given strain component, or combination of components, to be either fixed or constrained to map the energy landscape for a given deformation.

TBSM is an "affine shear" deformation method that homogeneously deforms systems with the boundary condition of fixing an atom in the system rather than a rigid block to handle translational invariance. As in RBSM, we calculate $U_N$ according to (2), but $N_a$ now denotes the number of molecules in the supercell. We report the TBSM convergence analysis for oxygen and anthracene in the supplementary material section S4. This investigation shows that for oxygen 12 layers in the supercell sheared at a strain per step equal to or less than 0.004 converges the strain-energy curve up to the point of slip. For anthracene, convergence was insensitive to the supercell size, while a strain step equal to or less than 0.01 is sufficient.

## 3. Results and Discussion

This section has two main parts. The first part investigates the deformation of oxygen in the (111) plane and the angular distortions of molecules. Then, we identify the slip barriers for the (110) and higher index planes and compare them to those barriers in (111). Amongst the variety of deformation mechanisms found, we focus on rotational twinning and relate it to the lattice parameters.

The second part deals with anthracene. Shearing the (001) plane provides a 2D barrier map of the various slip systems, that can then be compared against experimental data. A strong coupling of the molecular rotations with shear strain is found especially since anthracene contains two molecules in its unit cell. Further analysis of the deformation mechanisms uncovers rotational twinning in anthracene as well as three virtual polymorphs; polymorphs which are independently computed in-silico from experiment, one of which is likely to be the experimentally known but poorly characterised triclinic polymorph ANTCEN18.

### $\beta$-oxygen

**Shearing in the (111) plane.** Defect-free FCC metal nanowires deform by slip and/or twinning in the (111) plane[9]. $\beta$-oxygen has a similar (111) plane structure to FCC metals, except that molecules occupy lattice sites rather than atoms, leading to a strain energy that is dependent on the position of the centre of mass of molecules and the angular distortions (i.e., rotations of the molecules). RBSM and TBSM are both capable of precisely determining these quantities, as shown below. Both methods were applied to systems composed of twelve layers.

Figure 6 shows that the barrier, the highest normalised strain energy before the first slip event (characterised by a sudden energy drop), for (111)$[11\bar{2}]$ is lower than that for (111)$[10\bar{1}]$, for both RBSM and TBSM. The calculated barriers for the former slip direction are equal (0.020) while for the latter they are similar (0.026 for RBSM and 0.029 for TBSM). This slip system is also the lowest energy path found by GSFE calculations in FCC metals, and corresponds to the twinning direction; see Figure 5.4 in previous work.[9] The slip strain for (111)$[11\bar{2}]$ equals 0.15 when calculated using the two methods, while for the (111)$[10\bar{1}]$ RBSM gave a slip strain of 0.16, which is lower than 0.18 calculated using TBSM. Analysis of the trajectories shows that the deformation mechanism in RBSM along (111)$[10\bar{1}]$ (solid blue) always involved single slip events at the interface between regions 1 and 3, as shown in the supplementary material, Movie S5.1. The rationalisation for this will be highlighted when the angular distortions are discussed below. Note that the energy profile after each slip event is identical. In contrast, for TBSM the deformation mechanism following the first slip event along (111)$[10\bar{1}]$ produces stacking faults in the (111) plane. The second slipping event produces a change in the conventional cell representation, plus stacking defects in planes other than (111). Further strain annihilates such defects and the configuration adopts a different conventional cell representation from the starting one, and slip proceeds in a completely different slip system, see supplementary material Movie S5.2.

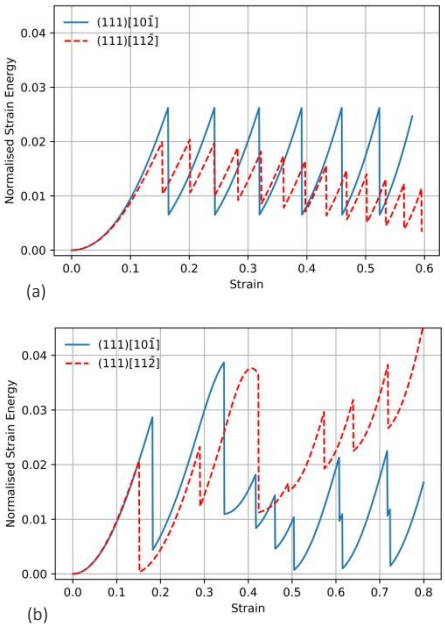


Figure 6: Normalised strain energy ($U_N$) as a function of strain for shearing the (111)[$10\bar{1}$] and (111)[$11\bar{2}$] directions of $\beta$-oxygen using (a) RBSM and (b) TBSM.

For deformation along (111)[$11\bar{2}$] (the twinning direction in FCC metals), using RBSM the sequence of events causes the layers to ultimately change their …**ABCABC…** stacking into **…BACBAC…** (i.e., slip via twinning is observed in molecular oxygen as is found for FCC metals and we will refer to this as the twinning direction in the detailed analysis below), see supplementary material Movie S5.3. TBSM produced a different deformation process to RBSM. Figure 6 (b) shows that the first two barriers, at strains 0.15 and 0.29, correspond to stacking fault emissions and/or twins across some interfaces. Subsequent barriers denote a change in the conventional cell representation and emission of defects and slip in completely different slip systems, see supplementary material Movie S5.4.

Angular distortions were investigated in terms of the inclination, $\delta$, and azimuth, $\theta$, angles. For the twinning direction, no change in $\theta$ occurred. Variation was observed in $\delta$ for both RBSM and TBSM, as shown in Figure 7, where the methods calculate the same peak for the change in inclination angle, $\Delta\delta$, of about 10.4°. $\Delta\delta$ was the same for all molecules in both methods, except for those that are part of the rigid blocks in RBSM which cannot rotate/move with respect to each other, and thus we plot only single curves in Figure 7.

Next, shearing (111)[$10\bar{1}$] in $\beta$-oxygen causes a change in $\delta$ and $\theta$ for both methods. Figure 8 shows that the angular distortion in TBSM is higher than for RBSM. Similar to the previous shear direction, the change in both angles and for both methods are homogeneous for all molecules. Two angular distortions are involved in (111)[$10\bar{1}$] slip; the non-zero $\Delta\delta$ means that molecules cannot maintain their orientation parallel to the *z* axis. Deformation movies along the slip direction showing the mentioned rotations are provided in supplementary material, Movies S5.1 and S5.5.

Angular distortions can help explain why RBSM and TBSM give different deformation mechanisms along the slip direction. In the (111) plane of $\beta$-oxygen, angular distortions occur homogeneously (to within a maximum of 1 %) for all molecules across all layers. For RBSM, the molecules in the rigid blocks are fixed and, consequently, their angular distortion has to be zero. This disparate distribution of angular distortions in the system gives rise to slip at the interface between regions 1 and 3, which is a limitation of methods where shear is driven by translation of rigid blocks. Hence, slip occurs at a

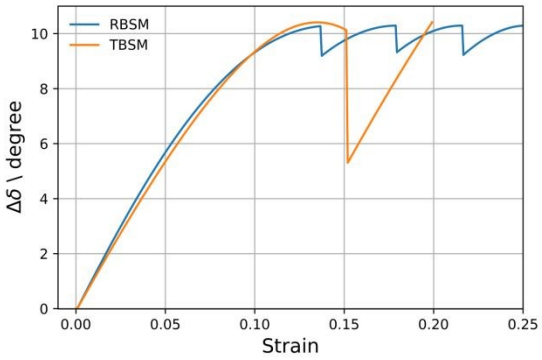


Figure 7: Change in the inclination angle $\delta$ as a function of strain when $\beta$-oxygen is sheared along the twinning direction by RBSM and TBSM.

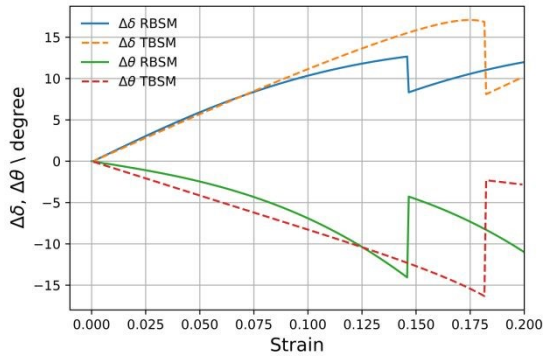


Figure 8: Change in the inclination and azimuth angles, $\delta$ and $\theta$, respectively, as a function of strain when $\beta$-oxygen is sheared along the slip direction by RBSM and TBSM.

lower barrier than for TBSM, where all molecules deform homogeneously, thus delaying the point at which instability occurs along the deformation path to a slip strain of 0.18, as compared to 0.16 calculated via RBSM. This also causes a conventional cell representation change that complicates the deformation.

**Deformation in the (110) and other high index planes.** Deformation simulations were performed in (110) and higher index planes in $\beta$-oxygen according to the notation defined in Figure 2, and the results are reported in Figure 9. Careful examination of the RBSM results in Figure 9 (a) shows that there exists a consistency in the ranking of the slip systems, sorted from lower to higher as “twin”, “45°”, “anti-twin”, “diagonal”, and lastly “135°”, except for the (113) plane where the “anti-twin” and the “diagonal” barriers are almost equal. In other words, we found a structure-property correlation in $\beta$

-oxygen where the RBSM shearing in the direction opposite to the molecular vector (i.e., see the dashed blue arrows Figure 2 (b)) yields the lowest slip barriers. Examining the TBSM barriers in Figure 9 (b) shows that, unlike RBSM, there is a more complicated ranking of the barriers amongst different slip systems. The "twin" and "45°" systems are still the easiest slip systems across the (110) and higher index planes, except for the "anti-twin" barrier changing this ranking for the (113) plane and higher. RBSM predicts that (113)[$\overline{3}\overline{3}2$] is the easiest slip system, while TBSM predicts (112)[$\overline{1}\overline{1}1$]. We note that the lowest strain energies for each slip plane are similar and that these predictions are consistent to within the difference in the angle between (113) and (112)[52], *i.e.* 13°, see supplementary material S6.

The RBSM and TBSM methods simulate two different types of experiment, *i.e.*, simple shear versus homogeneous shear. There are several barriers in the higher index planes of $\beta$-oxygen lower than the lowest barrier of 0.02 in (111). This shows that even though $\beta$-oxygen is characterised by close-packed (111) planes and exhibits similar plasticity to FCC Au, *e.g.* slip and twinning, its easiest slip systems nevertheless lie in higher index planes, which goes beyond the standard theory of dislocations.[8] This demonstrate that the additional variable, rotational distortion of $\beta$-oxygen molecules, strongly affects the predicted barriers and deformation outcomes.

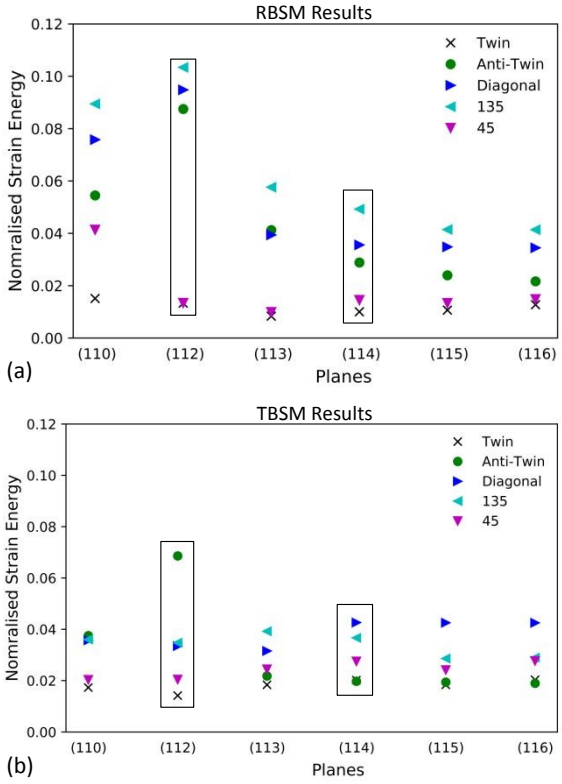


Figure 9: The normalised strain energy barriers across five different slip planes as labelled on the *x*-axis, for five different slip systems as per the legend, using (a) RBSM and (b) TBSM. The planes where annealing-induced twins were experimentally observed[25] are indicated with black rectangles surrounding the points.

**Rotational Twinning.** The theory for deformation twinning in FCC metals is relatively well-developed and the contributions of partial dislocations and stacking faults in the (111) plane are well-appreciated[53]. A computational procedure based on attachment energy calculations can predict the occurrence of reflection twinning in inorganic crystals,[54] assuming no internal relaxation occurs in the structure. Deformation twinning (of a rotational type) in calcite has been computationally investigated using molecular dynamics and is related to the rotation of carbonate.[55] During our investigation of $\beta$-oxygen, rotational twinning was found in the (110) and (112) planes along the "twin" directions using both RBSM and TBSM. Below, we limit our analysis to rotational twinning in (110). Figure 10 shows the normalised strain energy obtained by shearing in the (110)[001] ("twin") direction using RBSM and TBSM. Both methods produce a consistent evolution of strain energy. The first barrier is the highest, followed by progressively lower barriers in TBSM until all the structure twins and the normalised energy goes to zero, indicating that the structure is energetically equivalent to the starting structure, *i.e.*, a fully twinned structure has been reached. In contrast, for RBSM, as the twinning sequence approaches the rigid regions, the last two twinning events have relatively high barriers because of the interaction between the rigid blocks and the molecules in region 1. Figure 11 shows snapshots of rotational twinning based on two particular frames from Figure 10. Deformation movies can be found as supplementary material, Movies S7.1 and S7.2.

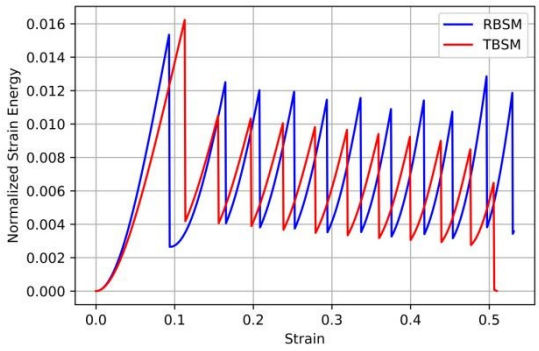


Figure 10: Normalised strain energy ($U_N$) as a function of strain for shearing in the (110)[001] direction of $\beta$-oxygen using RBSM and TBSM.

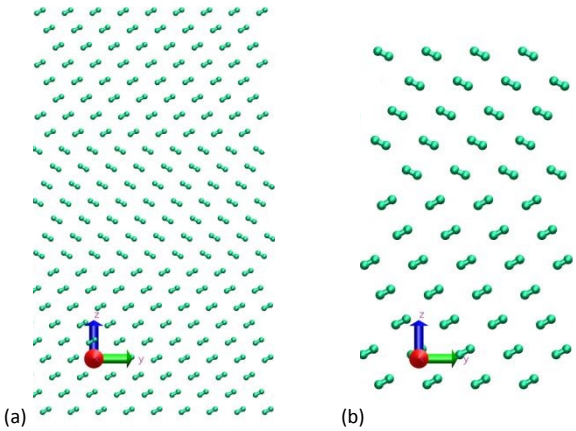

Figure 11: Snapshots of rotational twinning from Figure 10 for (a) RBSM at 0.34 strain and (b) TBSM at 0.32 strain where 7 layers have twinned.

Further insights regarding rotational twinning can be derived using a differential displacement analysis. Suppose we have a supercell or a surface cell of diatomic oxygen molecules with several layers where only a single molecule occupies each layer. Let the centre of mass of every molecule be calculated for the reference configuration and all the other strained configurations. It is then possible to calculate the displacement vector, $d_p^t$, of every molecule, *p*, for every deformed configuration, *t*. We can then define the differential displacement across the surface, *i*, between molecules *p* and *p+1* for frame *t* as;

$$\Delta d_i^t = d_p^t - d_{p+1}^t \ldots(\text{Å}) \quad (9)$$

$\Delta d_i^t$ is a geometric quantity that can capture the relative displacement across an interface and is used below (with superscript t removed for clarity) to investigate rotational twinning across all interfaces. Figure 12 (a) shows that the change in $\Delta d_i$ is heterogeneous across the interfaces between the zero-strain limit and the frame just before the instability. The first twinning event corresponds to a $\Delta\delta$ of 57.4° for molecules 6 and 7, as shown in Figure 12(b). The rotation of a single molecule affects $\Delta d_i$ of the layers above and below. Hence, as molecules 6 and 7 rotate, three $\Delta d_i$ jumps were recorded; $\Delta d_6$ and $\Delta d_8$ of 0.67 Å, and $\Delta d_7$ with 1.35 Å (twice the single contribution from molecules 6 and 7). As the

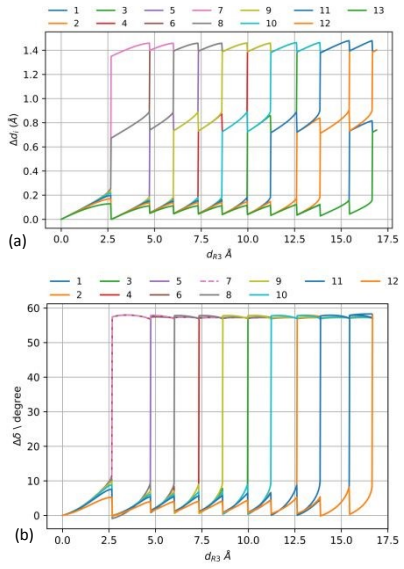


Figure 12: RBSM rotational twinning analysis plot using the differential displacement $\Delta d_i$ in (a), and change in inclination angle $\Delta\delta$ in (b), as a function of the shear displacement of region 3 $d_{R3}$, sheared in the (110)[001] direction. Indices i in $\Delta d_i$ correspond to; 1, the differential displacement at the surface bounded by region 3 and the first molecule in region 1, 2, the surface at the interface between molecules 1 and 2 in region 1, etc. The legend in (b) corresponds to the indices of the molecules with 1, the first molecule in region 1 at the interface with region 3, and 12 the last molecule in region 1 at the interface with region 2.

structure is further strained, more molecules rotate and sudden jumps in $\Delta d_i$ are recorded, until all the molecules are rotated. All the differential displacements equal 1.38 Å, except for the molecules in the rigid blocks and interface layers 1 and 13, i.e., between the rigid blocks and region 1. In order to explain the crystallographic origin of the differential displacements, we recall the lattice parameters of the unit cell used to simulate the (110) plane (in Å);

$$\vec{a} = 3.3332\,\hat{j} \quad (10.1)$$

$$\vec{b} = -4.0735\,\hat{i} \quad (10.2)$$

$$\vec{c} = 1.3461\,\hat{i} + 5.0884\,\hat{k} \quad (10.3)$$

where $\hat{i}$, $\hat{j}$, and $\hat{k}$ are the Cartesian unit vectors. The *x* component of the lattice vector *c* is equal to the first jump in $\Delta d_7$ (1.35 Å), showing that rotational twinning is not related to the Burgers vector or dislocations but rather to crystallography and symmetry operations. TBSM produced similar results to RBSM. Both RBSM and TBSM predict rotational twinning in (112)[$\bar{1}\bar{1}1$] with similar results as previously shown. A secondary relaxation procedure; where every strained configuration had all constraints removed and the energy the structure was minimised to reach the corresponding energy minimum, was used to compute the twinning interfacial energies ($\gamma_T$ ), and are reported in Table 2.

Table 2: Twinning interfacial surface energy ($\gamma_T$ mJ/m²) for the slip systems of $\beta$-oxygen that show rotational twinning, calculated for both RBSM and TBSM structures.

| $\gamma_T$ | RBSM | TBSM |
|---|---|---|
| (110)[001] | 3.6 | 3.6 |
| (112)[$\bar{1}\bar{1}1$] | 3.0 | 3.2 |

RBSM and TBSM provide critical insights into the nature and occurrence of rotational twinning in molecular crystals. The energetics of rotational twinning look very similar to the twinning of FCC metals in the (111) plane [56] and the non-rotational twinning we found in the (111) plane of $\beta$-oxygen. Most importantly, rotational twinning involved the stacking lattice parameter, *c*, and is thus governed by the lattice symmetry rather than partial dislocations. Our results extend the observations of annealing-induced rotational twins in experiments on solid $O_2$ [25] and show that shear deformation should also be able to produce such twins.

### Anthracene

**Normalised strain energy barriers.** Previous experiments have shown that anthracene deforms in (001)[110] and (001)[010][19,20]. Transmission electron microscopy (TEM) has been very successful in enabling the direct observation and characterisation of linear (dislocations) and planar (stacking faults, twinning) faults in crystalline materials, particularly in metals.[57] Few comparable studies have been reported on organic crystalline materials because of their extreme sensitivity to electron-induced radiation damage. Here we directly identify the most common basal slip systems in anthracene induced by mechanical deformation, made possible by cooling the specimens with liquid helium. Electron diffraction patterns showed that the large crystal face of the samples was (001), and the goniometer stage allowed this to be oriented approximately perpendicular to the direction of the electron beam +/- $25^0$. Gentle

bending of the crystals whilst attached to the TEM grids induced slip, primarily on (001), through the introduction of dislocations, with their density increasing with an increasing amount of deformation, as illustrated in Figure 13. Through the use of bright field and dark field imaging, *i.e.* imaging with the central diffraction beam, or one diffracted from specific, identified crystallographic planes, the slip systems of various dislocations were characterised. When a dark field image is formed using an electron beam diffracted from planes that are not perturbed by a particular dislocation, the dislocation will not be seen in a dark field, whilst it is visible in bright field.

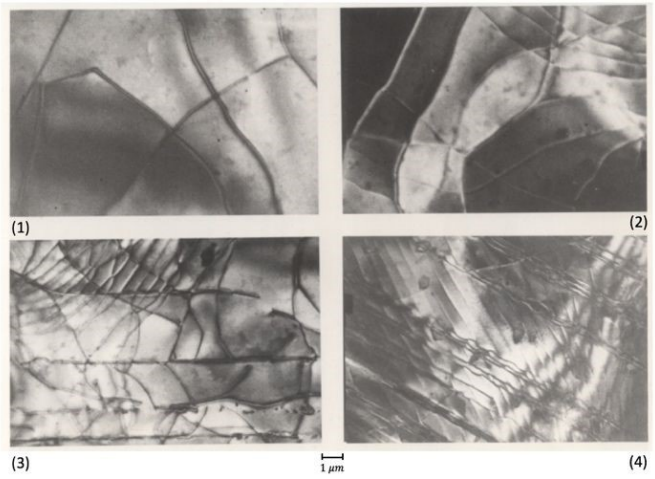


Figure 13: Dislocations observed via TEM in the basal plane of anthracene. Images numbered 1 to 4 correspond to increasing deformation of the crystal.

Mathematically this is described by the relationship g.b = 0, where g is the Miller index of the crystal planes used to form the dark field image and b is the Burgers vector of the dislocation. An example is shown in Figure S8.2.1, supplementary material S8. From the study of many anthracene crystals, the basal slip systems that were identified are: (001)[110],(001)[010], (001)[100}, and (001)[$\bar{1}$20]. The last two were previously unknown.

This section applies RBSM and TBSM to anthracene to verify these results. Figure 14 shows the normalised strain energy barriers obtained from RBSM (crosses) and TBSM (solid circles) for several slip systems in the (001) plane of anthracene. The barriers form into two groups. The first have a low slip barrier of less than $\approx 0.2$, while the second barrier set is above 0.25, indicating the latter slip systems are more difficult to activate. In contrast to molecular oxygen, there are significant differences between the barriers calculated using RBSM and TBSM. The latter method calculates the barriers for the four observed slip directions to be the four lowest. However, the former approach predicts that (001)[$\bar{1}$20] has the highest barrier, and the three highest barriers are all close to each other, in contrast to TBSM. Our experimental results are based on bending of anthracene crystals which emulates a "pure shear" deformation, similar to the shear deformation applied via TBSM, unlike RBSM which emulates a different experiment. This leads to the observed consistency between our computational and experimental results.

**Deformation mechanisms in anthracene.** Slip deformation mechanisms in anthracene are more complicated than in diatomic oxygen. Figure 15 shows the normalised strain energy of RBSM deforming two anthracene surface cells, having 10 and 16 layers in region 1, in the (001)[010] system. As the system is sheared, the strain energy increases and couples to rotational deformation of molecules, which becomes very complicated beyond the point of slip. The maximum rotational deformation of anthracene molecules corresponds to -16° rotation about the *y*-axis with lesser rotations about the *x*-axis and the *z*-axis.

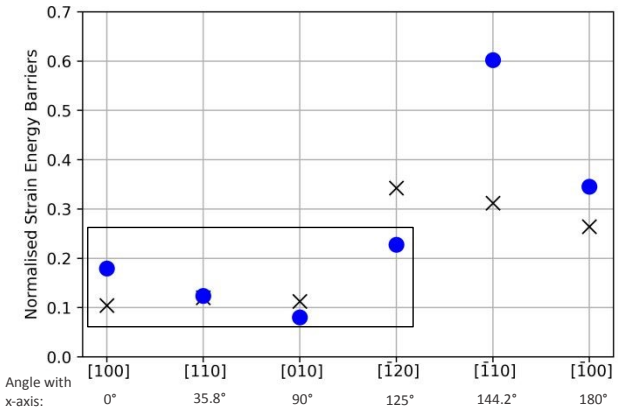


Figure 14: Slip barriers obtained via RBSM (crosses) and TBSM (solid circles) for the slip systems indicated on the x-axis in the (001) plane of anthracene. The rectangular box denotes the experimentally observed slip systems. The angle below the x-axis represents the angle between the crystallographic direction and the x-axis in the anthracene surface cell.

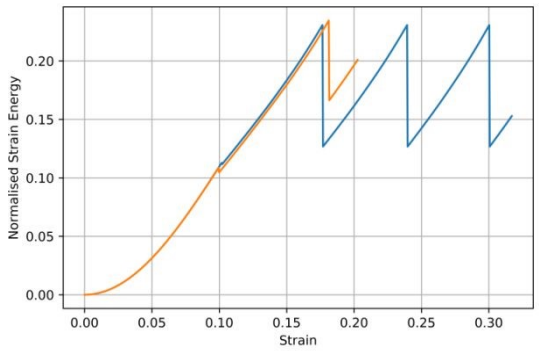


Figure 15: Normalised strain energy as a function of strain for shearing the (001)[010] system in anthracene using RBSM for system sizes of ten (blue) and sixteen (orange) layers.

The detailed discussion of the deformation aspects of this slip system and angular distortions are found in supplementary materials section S9; deformation movie S9.5. Figure 16 shows the deformed system just before slip for the 10 layers simulation where the deformation induced rotations of molecules close to the mid-section of the surface cell are magnified compared to selected molecules from region 2 that represent the molecular orientations in the bulk phase. TBSM shearing of (001)[010] leads to a series of polymorphic transitions that we discuss below. Supplementary material S9.4 shows that the molecular rotations of anthracene in the supercell are

consistent with those found in RBSM; Figure 17 shows the deformed structure just before the transition. These deformation-induced molecular rotations indicate that whether homogeneous (TBSM-like) or displacement-type (RBSM-like) shear deforms the system in (001)[010], the angular distortions seem universal, although the slip state calculations lead to different outcomes for RBSM and TBSM; *i.e.* slip versus polymorphic transition, respectively.

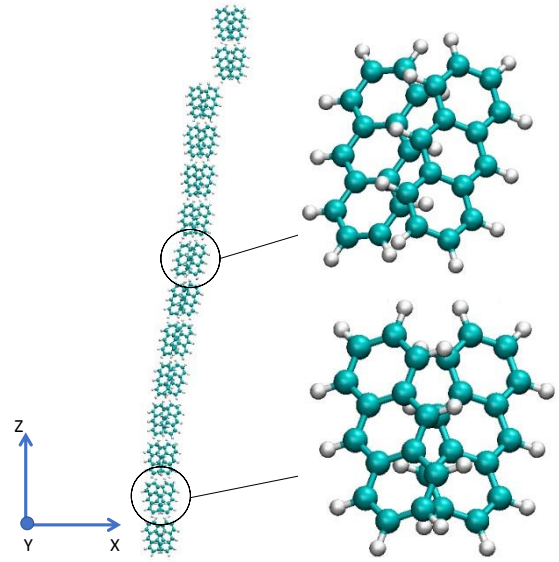


Figure 16: Image of the deformed structure of anthracene just before slip when sheared via RBSM in (001)[010]; the *z*-axis is perpendicular to (111) and the *x*-axis is parallel to [010]. The images of two sets of molecules are enlarged to show the rotation of molecules in layer 6 relative to the bulk molecules. The *y*-axis points into the page.

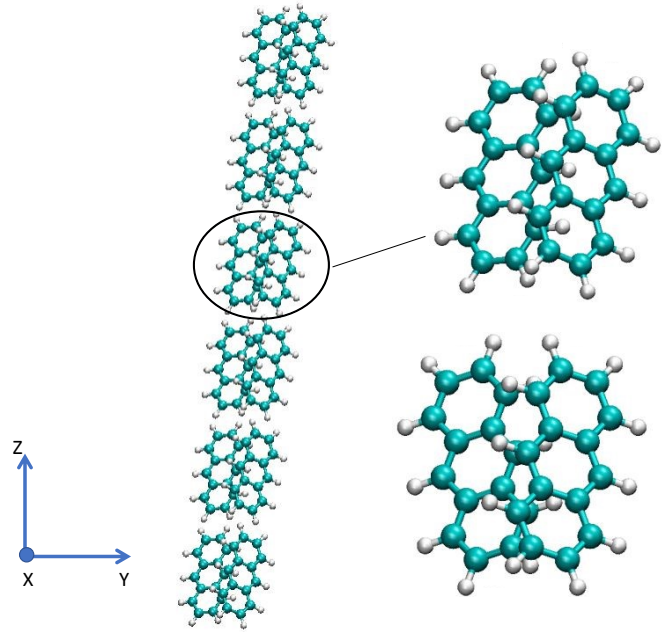


Figure 17: Image of the anthracene supercell just before the polymorphic transition when sheared via TBSM in (001)[010]; [010] is parallel to *y*-axis. One set of molecules indicated in the figure have their image magnified to show the molecular rotations; the other set represents molecules at zero strain. The *x*-axis points out of the page.

Shearing the (001)[110] system using RBSM shows that the system undergoes rotational twinning deformation, with the energies and important molecular rotations plotted in Figure 18.

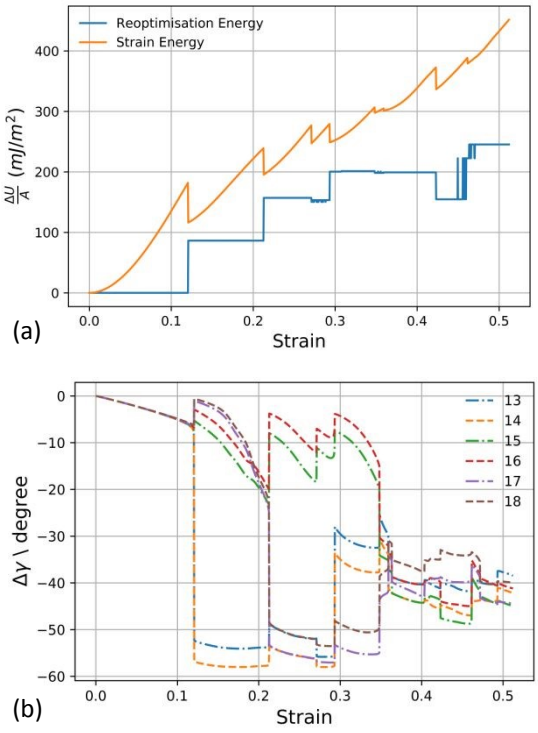


Figure 18: Results show the rotational twinning observed in a ten-layer anthracene surface cell when sheared via RBSM along (001)[110]. (a) Strain and re-optimisation surface energies as a function of strain, (b) change in $\gamma$ (rotation about x) as a function of strain for selected molecules numbered as per the legend.

The strain energy increases due to shear and all the molecules in region 1 rotate (where for simplicity we only show a few molecules in Figure 18 (b)) until a first slip event happens, which corresponds to the rotation of molecules 13 and 14 by $\approx$ 55° clockwise about the *x*-axis, and the different angular relaxation of the other molecules. Upon performing secondary relaxation, the system relaxes to a configuration with one layer (two molecules) rotated and a relaxed twinning interfacial energy of 86 mJ/m$^2$. Subsequent straining of the structure creates more deformation twins as evident in Figure 18; slip beyond the second barrier produces another layer of rotated molecules because molecules 17 and 18 show a sudden jump in $\Delta\gamma$ and the re-optimisation energy becomes 157 mJ/m$^2$. The deformation movie and additional information regarding this rotational twinning in anthracene are found in supplementary material Movie S10.1 and Figure S10.2. As expected, the complexity of deformation twinning in anthracene exceeds that of metals and diatomic oxygen since several events contribute to the process. Figure 18 shows that that anthracene hinders rotational twinning deformation, *i.e.*, subsequent barriers increase and so do the energies of the re-optimised configurations. Second, rotational twinning deformation in anthracene involves three Eulerian angles in contrast to diatomic oxygen involving a single angle, *i.e.* anthracene

View Article Online
DOI: 10.1039/D2CE01436F

molecules in the twinned region rotate with respect to each other beyond reflection. This complexity implies the system has a tendency to find local meta-stable structures and defects as a consequence of twinning deformation Our re-optimised structure and energies analyses indicate that the twinning interfacial energy, $\gamma_T$, in anthracene is approximately 245 $\pm$ 22 mJ/m$^2$.

Rotational twinning deformation was not only found in (001)[110], but also in (001)[100], as shown in supplementary material Movie S11.1 and Figure S11.2. This rotational twinning is similar to that in (001)[110], with $\gamma_T$ of a four-layer rotated configuration in (001)[100] of 171 mJ/m$^2$, which is lower than the twinning interfacial energy of the same twin size in (001)[110] of 211 mJ/m$^2$. TBSM shearing of (001)[100] and (001)[110] leads to a series of polymorphic transition events; these will be the subject of the next section.

**Mechanically-induced polymorphic transitions.** TBSM shearing of the slip systems (001)[110] and (001)[100] both result in the same polymorphic transitions, as shown in supplementary material Figure S12.1, where both systems display the same two higher energy structures after re-optimisation. For both slip systems, TBSM shear increases the strain energy until the first slip events happen; (001)[110] at 0.2 strain slips into virtual polymorph 1 (Po1) having a relative stability ($\Delta$U) of +1.6 kJ/mol in comparison to the initial structure, while (001)[100] slips into the same virtual polymorph at 0.36 strain. Further TBSM shearing of both slip systems leads to a transition into virtual polymorph 2 (Po2) having a $\Delta$U of +3.2 kJ/mol. Just as RBSM predicts the same deformation mechanism (which does not involve polymorphs) for the (001)[110] and (001)[100] systems, TBSM predicts the same polymorphic transitions.

Contrary to the polymorphic transitions in (001)[110] and (001)[100], TBSM shearing of (001)[010] gives a unique virtual polymorphic transition path. Supplementary Material Figure S12.2 shows that the first slip event transforms the system into the virtual polymorph Po1 identified in the previous slip with a $\Delta$U of +1.6 kJ/mol. Subsequent straining of this configuration leads to a series of structures having defects, *i.e.*, every sharp drop of the internal energy in Figure S12.2 other than the first emits one or more defects through the structure until all the interfaces have faults. By then, the system completely transforms into a third virtual polymorph (Po3) with $\Delta$U of +3.4 kJ/mol. supplementary material Movie S12.3 shows the associated deformation trajectory. This result of TBSM leading to full polymorphic transitions in the (001)[110] and (001)[100] directions, compared to sequential transitions events seen in (001)[010], encouraged us to repeat the optimisations of the virtual polymorphs using a more accurate level of theory (DFT-D), see supplementary materials S13.

Table 3 reports the density functional theory (DFT) and force field (FF) calculations for the reference experimental structure and the other virtual polymorphs. The order of relative stability is different between the force field, which ranks Po0<Po1<Po2<Po3, while DFT gives the order Po0<Po1<Po3<Po2. The discrepancy in the lattice parameters between DFT and FF for all the configurations is below 3 % except for Po3, where the error in $\alpha$ is 5.6 %, which shows that DFT and FF calculations provide similar structures for anthracene. The structure files (.cif and .gin) of the polymorphs can be found as supplementary material.

RMSD15[58] analysis, a standard technique in the literature to identify unique polymorphs, was conducted for the polymorph structures in Table 3, with the experimental structure (energy minimum used herein) as the reference. The maximum number of molecules that could be overlaid were 9 between Po1 and the experimental structure, as found using both FF and DFT configurations. Supplementary material Table S14.1 provides further details about the RMSD15 analysis. The outcome is that all the virtual polymorphs found are unique with respect to the reference configuration. Figure 19 shows representative molecules of the overlay of the virtual polymorphs upon the experimental configuration. Indeed, there have been significant studies on the mechanically-induced polymorphic transitions in anthracene. The reference structure used in our calculations, which was shown different compared to the virtual polymorphs, was compared against all anthracene structures reported in the Cambridge Crystallographic Database (code ANTCEN) and were found to be equivalent, see supplementary materials S14, implying that none matches our virtual polymorphs except ANTCEN18 which is a triclinic polymorph discovered by Parkinson *et al.* [59] via experiment. This experiment was only able to determine the lattice parameters. Further computational investigation[60,61] predicted the lattice parameters and coordinates of a physically stable anthracene configuration to within $\pm$5 % error of the experimental structure. The authors[61] suggest that anthracene polymorph (ANTCEN18) has the re-defined lattice parameters compared to those in Cambridge Crystallographic Database of 8.342 Å, 5.892 Å, 9.430 Å, 91.88°, 95.45 °, and 85.91°, for $a$, $b$, $c$, $\alpha$, $\beta$, $\gamma$, respectively, and $\Delta$U of 2 kJ/mol, which is within the range of, yet distinct from, the values for our reported polymorphs; see Table 3. This is perhaps due to the lack of symmetry in triclinic systems implying that there is no single unique unit cell that defines the crystallography. However, RMSD15 analysis of the structure having the above lattice parameters and its corresponding internal coordinates[61] as a reference versus our polymorphs indicated that 15 molecules could be overlaid only for Po2. Thus, TBSM predicts a polymorph suggested in the literature as ANTCEN18[59,60,61], and that this polymorph is preceded by Po1 and is obtainable via shear of the (001)[100] or (001)[110]. Rizzato *et al.* have shown that molecular dynamics anisotropic compression of anthracene leads to a phase transition into a polymorph[37], which is compared here using RMSD15 with Po1, Po2, and Po3, showing that 7 (0.66 Å RMS), 7 (1.078 Å RMS), and 5 (2.582 Å RMS) molecules could be overlaid, respectively; thus differing from the virtual polymorphs reported here.

Our analysis of the deformation mechanisms in anthracene shows that displacement shear leads to complicated deformation outcomes that involve rotational degrees of freedom of the molecules. The finding of rotational twinning resulting from displacement shear

View Article Online
DOI: 10.1039/D2CE01426F

imposed by RBSM for the (001)[110] and (001)[100], or the polymorphic transitions resulting from homogeneous shear enforced by TBSM for the same slip systems, suggest that the tilt boundaries, indicated by Robinson and Scott[40], might originate from these phenomena instead of partial dislocations. Our proposed polymorph formation in anthracene via shear may resolve the outstanding issue as to whether anthracene has polymorphs or not[33, 37, 41, 59, 60, 62, 63] and suggest to experimentalists the slip systems that need to be sheared to obtain these polymorphs.

## 4. Conclusion

Our methods predict the ranking of the slip systems in β-oxygen across several low and high index planes. β-oxygen has a close-packed <111> direction similar to FCC metals, yet the easiest slip system was found in higher-index planes; (112) and (113) according to RBSM and TBSM, respectively, with the "twin" direction as the easiest direction of slip. In the (111) plane, RBSM and TBSM found the same homogeneous change in azimuth and inclination angles of oxygen molecules when sheared along the slipping and twinning directions. Because RBSM has rigid blocks and molecules that cannot rotate, slip always happens at the interface between the rigid and relaxed regions. On the other hand, the TBSM barrier along the slipping direction is higher than that in RBSM because TBSM requires more energy to adjust the internal degrees of freedom and thus slips at higher strain. Furthermore, TBSM shear could slip the system along new directions by changing the cell representation after slip, which is not possible in the case of RBSM. This critical result highlights essential features of homogeneous shear methods ("pure shear") compared to displacement shear methods ("simple shear").

Table 3: Summary of the lattice parameters and relative stability ($\Delta U$) with reference to the experimental structure of the several polymorphs of anthracene calculated using density functional theory (DFT), GAFF force field (FF)[35], and Williams IVa force field (FF*) [64].

| Theory | Polymorph | *a* (Å) | *b* (Å) | *c* (Å) | $\alpha$° | $\beta$° | $\gamma$° | $\Delta U$(kJ/mol) |
|---|---|---|---|---|---|---|---|---|
| DFT | 0 (Exp.) | 8.5140 | 5.9762 | 11.1877 | 90.00 | 124.60 | 90.00 | 0 |
| FF | 0 (Exp.) | 8.2570 | 5.9290 | 10.9143 | 90.00 | 124.48 | 90.00 | 0 |
| DFT | 1 | 7.9463 | 5.9937 | 10.954 | 99.96 | 114.24 | 86.25 | 0.2 |
| FF | 1 | 7.8459 | 5.8390 | 10.8395 | 98.73 | 114.96 | 86.76 | 1.6 |
| DFT | 2 | 7.9369 | 6.1084 | 9.8380 | 96.72 | 93.74 | 94.72 | 1.7 |
| FF | 2 | 7.8371 | 5.9823 | 9.6028 | 95.42 | 90.78 | 94.89 | 3.2 |
| DFT | 3 | 7.8059 | 6.2200 | 11.2541 | 63.93 | 107.50 | 95.14 | 0.9 |
| FF | 3 | 7.6476 | 6.0423 | 11.1659 | 67.51 | 110.03 | 94.44 | 3.4 |
| FF* | ANTCEN18 | 8.3420 | 5.8920 | 9.4300 | 91.88 | 95.45 | 85.91 | 2 |

View Article Online
DOI: 10.1039/D2CE01426B

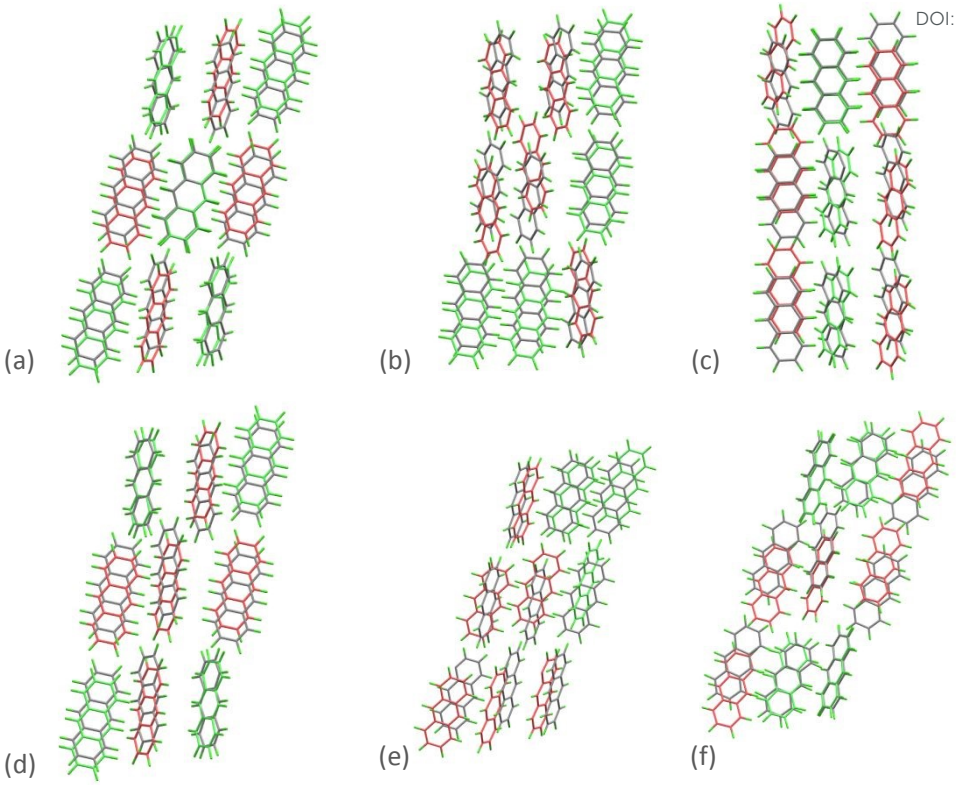


Figure 19: Overlay of the molecules of anthracene polymorphs (carbon rings coloured in grey for successful overlays and in red for unmatched molecules) over the molecules of the experimental configuration (carbon rings coloured in green) obtained from RMSD15 analysis. (a) (b) and (c) represent configurations calculated using FF, for the Po0-Po1, Po0-Po2, and Po0-Po3 overlays, respectively, while (d), (e), and (f) represent configurations calculated using DFT for the same sequence of comparison.





Our *in-silico* shear experiments on oxygen couple shear deformation with molecular rotations ranging from about 57°, characteristic of rotational twinning in (110), to a few degrees along other slip systems. We find rotational twinning using RBSM and TBSM, whereby twinning occurs via molecule rotation. No dislocations are involved in rotational twinning, rather the lattice symmetry.

Rotational twinning was only obtained for two slip systems, in the (110) and (112) planes, while the remainder of the higher index planes sheared along the "twin" direction produced extended and orthogonal defects. This complex defect landscape implies that rotational twinning might not be easily predicted based only on the reference geometry, hence quasi-static methods are important. Given the slip barriers in β-oxygen and the dominance of the "twin" system, we anticipate it has a poor and limited mechanical performance, though given the conditions under which this solid exists this is unlikely to be an issue.

Simulation of shear deformation of anthracene molecular crystals in the basal plane provided a range of barriers for slip systems. The easiest slip systems according to TBSM are (001)[100], (001)[110], (001)[010], and (001)[$\bar{1}$20], consistent with our TEM experiments of the active slip systems; the bending deformation in TEM matches the homogeneous "pure shear" simulated by TBSM. RBSM predicts the same results, except for (001)[$\bar{1}$20] being an inactive slip system, which suggests that "simple shear" and "pure shear" methods give similar, but not equivalent, deformation outcomes. Deformation mechanisms were far more complicated in anthracene than in oxygen. RBSM predicted slip deformation across the (001)[010] system, and rotational twinning for (001)[110] and (001)[100]. Slip in anthracene involved complex molecular rotations in three dimensions since the unit cell has two asymmetric molecules per layer (A and B), although single slip systems were probed one at a time. Such rotations were quantified and found to be very important, *i.e.* not only the differential displacement determines the internal energy but also the rotations of the molecules. TBSM analysis of the deformation mechanisms in anthracene revealed a variety of polymorphic transitions along (001)[010], (001)[100], and (001)[110]. Two new and one experimentally known polymorphs were identified and their relative stabilities and lattice parameters quantified; these polymorphs are energetically similar. In order to crystallise the existing polymorph (ANTCEN18), TBSM suggests that homogeneous shear of either the (001)[110] or (001)[100] systems is required, while noting that the low energy polymorph 1 (Po1) crystallises before polymorph 2 (Po2, ANTCEN18 equivalent). Sequential transitions from Po1 to Po3 were observed via a series of interfacial defects, while deformation energetics are similar to rotational twinning. Our results indicate that the tilt boundaries observed experimentally in anthracene could be related to polymorphs and/or twins rather than partial dislocations. The

prediction of facile slip across four systems in anthracene may lead to some degree of slip deformation; however, the finding of rotational twins and polymorphic transitions indicate that its tabletability might be difficult.

RBSM and TBSM had been applied to relatively simple molecular crystals, namely a diatomic molecule and a planar flat molecule, without conformational degrees of freedom. These molecular crystals demonstrate a coupling between the shear deformation and the rotations of the molecules that needs to be properly accounted for, beyond the metrics specified by dislocation theory, to predict the active slip systems. Although force fields were used to simulate slip, the use of a higher level of theory validated some of our findings. Furthermore, it would be interesting to experimentally verify the predictions regarding slip in diatomic oxygen and anthracene and their polymorphic transitions. Theoretically, the methods proposed here should be capable of simulating slip barriers and slip deformation in more complicated systems with torsional degrees of freedom coupled with shear deformation.

## Conflicts of interest

There are no conflicts to declare.

## Acknowledgements

MSH thanks Curtin University for providing a PhD scholarship, and Curtin Publication Grant, as well as AstraZeneca R&D Sweden for providing financial support. VMC thanks the European Union's Horizon 2020 research and innovation programme under the Marie Sklodowska-Curie grant agreement for funding under grant No 777778 (MATHROCKS). JDG thanks the Australian Research Council for funding under grant FL180100087. The provision of computational resources by the Pawsey Supercomputing Centre and National Computational Infrastructure is acknowledged. The TEM data on anthracene was obtained during a PhD project (GMP) in the Department of Metallurgy (now Materials) at the University of Oxford.

## References

1. X. Cao, M. Morganti, B. C. Hancock and V. M. Masterson, *J Pharm Sci*, 2010, **99**, 4307-4316.
2. S. Finnie, K. V. R. Prasad, D. B. Sheen and J. N. Sherwood, *Pharmaceutical research*, 2001, **18**, 674-681.
3. W. Connick and F. G. J. May, *Journal of crystal growth*, 1969, **5**, 65-69.
4. P. M. Robinson and H. G. Scott, *Molecular crystals and liquid crystals (1969)*, 1970, **11**, 13-23.
5. J. S. K.-L. Gibson, R. Pei, M. Heller, S. Medghalchi, W. Luo and S. Korte-Kerzel, *Materials*, 2021, **14**, 407.
6. L. Wang, Z. Zheng, H. Phukan, P. Kenesei, J. S. Park, J. Lind, R. M. Suter and T. R. Bieler, *Acta Materialia*, 2017, **132**, 598-610.
7. K. Abbasi, D. Wang, M. A. Fusella, B. P. Rand and A. Avishai, *Microscopy and Microanalysis*, 2018, **24**, 420-423.
8. J. P. Hirth and J. Lothe, *Theory of dislocations*, Wiley New York, 1982.
9. D. Hull and D. J. Bacon, in *Introduction to Dislocations (Fifth Edition)*, eds. D. Hull and D. J. Bacon, Butterworth-Heinemann, Oxford, 2011, DOI: https://doi.org/10.1016/B978-0-08-096672-4.00005-0, pp. 85-107.
10. C. R. Weinberger, B. L. Boyce and C. C. Battaile, *International Materials Reviews*, 2013, **58**, 296-314.
11. T. B. Britton, F. P. E. Dunne and A. J. Wilkinson, *Proceedings of the Royal Society A: Mathematical, Physical and Engineering Sciences*, 2015, **471**, 20140881.
12. J. Amodeo, S. Merkel, C. Tromas, P. Carrez, S. Korte-Kerzel, P. Cordier and J. Chevalier, *Crystals*, 2018, **8**, 240.
13. K. Kojima, *Progress in Crystal Growth and Characterization of Materials*, 1992, **23**, 369-420.
14. H. G. Gallagher, P. J. Halfpenny, J. C. Miller, J. N. Sherwood, J. E. Field and P. Gray, *Philosophical Transactions of the Royal Society of London. Series A: Physical and Engineering Sciences*, 1992, **339**, 293-303.
15. P. Hartman and P. Bennema, *Journal of Crystal Growth*, 1980, **49**, 145-156.
16. C. C. Sun and Y. H. Kiang, *Journal of Pharmaceutical Sciences*, 2008, **97**, 3456-3461.
17. V. Vítek, *The Philosophical Magazine: A Journal of Theoretical Experimental and Applied Physics*, 1968, **18**, 773-786.
18. K. Mirsky and M. D. Cohen, *Journal of the Chemical Society, Faraday Transactions 2: Molecular and Chemical Physics*, 1976, **72**, 2155-2163.
19. P. M. Robinson and H. G. Scott, *Acta Metallurgica*, 1967, **15**, 1581-1590.
20. K. Kojima, *phys. stat. sol. (a)*, 1979, **51**, 71-78.
21. L. B. Munday, S. D. Solares and P. W. Chung, *Philosophical Magazine*, 2012, **92**, 3036-3050.
22. N. Mathew and T. D. Sewell, *Philosophical Magazine*, 2015, **95**, 424-440.
23. L. M. LeBlanc, A. Otero-de-la-Roza and E. R. Johnson, *Crystal Growth & Design*, 2016, **16**, 6867-6873.
24. R. S. Hong, E. J. Chan, L. Vogt-Maranto, A. Mattei, A. Y. Sheikh and M. E. Tuckerman, *Crystal Growth & Design*, 2021, **21**, 886-896.
25. J. Venables, C. English, K. Niebel and G. Tatlock, *Journal de Physique Colloques*, 1974, **35**, C7-113-C117-119.
26. Y. A. Freiman and H. J. Jodl, *Physics Reports*, 2004, **401**, 1-228.
27. K. Kobashi, M. L. Klein and V. Chandrasekharan, *The Journal of Chemical Physics*, 1979, **71**, 843-849.
28. J. C. Laufer and G. E. Leroi, *The Journal of Chemical Physics*, 1971, **55**, 993-1003.
29. G. E. Jelinek, L. J. Slutsky and A. M. Karo, *Journal of Physics and Chemistry of Solids*, 1972, **33**, 1279-1290.
30. J. G. Powles and K. E. Gubbins, *Chemical Physics Letters*, 1976, **38**, 405-406.
31. A. Kelly and K. M. Knowles, in *Crystallography and Crystal Defects*, 2012, DOI: https://doi.org/10.1002/9781119961468.ch1, pp. 1-41.
32. K. Momma and F. Izumi, *Journal of Applied Crystallography*, 2011, **44**, 1272-1276.
33. A. J. Cruz-Cabeza, N. Feeder and R. J. Davey, *Communications Chemistry*, 2020, **3**, 142.
34. R. Mason, *Acta Crystallographica*, 1964, **17**, 547-555.

35. J. Wang, R. M. Wolf, J. W. Caldwell, P. A. Kollman and D. A. Case, *J Comput Chem*, 2004, **25**, 1157-1174.
36. M. J. Frisch, G. W. Trucks, H. B. Schlegel, G. E. Scuseria, M. A. Robb, J. R. Cheeseman, G. Scalmani, V. Barone, G. A. Petersson, H. Nakatsuji, X. Li, M. Caricato, A. V. Marenich, J. Bloino, B. G. Janesko, R. Gomperts, B. Mennucci, H. P. Hratchian, J. V. Ortiz, A. F. Izmaylov, J. L. Sonnenberg, Williams, F. Ding, F. Lipparini, F. Egidi, J. Goings, B. Peng, A. Petrone, T. Henderson, D. Ranasinghe, V. G. Zakrzewski, J. Gao, N. Rega, G. Zheng, W. Liang, M. Hada, M. Ehara, K. Toyota, R. Fukuda, J. Hasegawa, M. Ishida, T. Nakajima, Y. Honda, O. Kitao, H. Nakai, T. Vreven, K. Throssell, J. A. Montgomery Jr., J. E. Peralta, F. Ogliaro, M. J. Bearpark, J. J. Heyd, E. N. Brothers, K. N. Kudin, V. N. Staroverov, T. A. Keith, R. Kobayashi, J. Normand, K. Raghavachari, A. P. Rendell, J. C. Burant, S. S. Iyengar, J. Tomasi, M. Cossi, J. M. Millam, M. Klene, C. Adamo, R. Cammi, J. W. Ochterski, R. L. Martin, K. Morokuma, O. Farkas, J. B. Foresman and D. J. Fox, *Journal*, 2016.
37. S. Rizzato, A. Gavezzotti and L. Lo Presti, *Crystal Growth & Design*, 2020, **20**, 7421-7428.
38. A. Gavezzotti, *New Journal of Chemistry*, 2011, **35**, 1360-1368.
39. P. M. Robinson and H. G. Scott, *Journal of Crystal Growth*, 1967, **1**, 187-194.
40. P. M. Robinson and H. G. Scott, *physica status solidi (b)*, 1967, **20**, 461-471.
41. R. Resel, M. Oehzelt, K. Shimizu, A. Nakayama and K. Takemura, *Solid State Communications*, 2004, **129**, 103-106.
42. A. Banerjee, N. Adams, J. Simons and R. Shepard, *The Journal of Physical Chemistry*, 1985, **89**, 52-57.
43. V. M. Segal, *Materials Science and Engineering: A*, 2002, **338**, 331-344.
44. S. Fleming and A. Rohl, *Journal*, 2005, **220**, 580.
45. J. D. Gale and A. L. Rohl, *Molecular Simulation*, 2003, **29**, 291-341.
46. D. E. Parry, *Surface Science*, 1975, **49**, 433-440.
47. *Surface Science*, 1976, **54**, 195.
48. P. Raiteri, 2021 https://github.com/praiteri/GPTA.
49. P. P. Ewald, *Annalen der Physik*, 1921, **369**, 253-287.
50. N. J. K. Withey, DOI: https://www.reading.ac.uk/maths-and-stats/-/media/project/uor-main/schools-departments/maths/documents/naomi-withey.pdf?la=en&hash=D4E67B2C7950B6520A098C189A0F5708, UNIVERSITY OF READING, 2012.
51. C. R. Weinberger and W. Cai, *Journal of Materials Chemistry*, 2012, **22**, 3277-3292.
52. C. Tannous, *European Journal of Physics*, 2019, **41**, 015501.
53. Y. T. Zhu, X. Z. Liao and X. L. Wu, *Progress in Materials Science*, 2012, **57**, 1-62.
54. S. D. Fleming, G. M. Parkinson and A. L. Rohl, *Journal of Crystal Growth*, 1997, **178**, 402-409.
55. A. S. Côté, R. Darkins and D. M. Duffy, *Physical Chemistry Chemical Physics*, 2015, **17**, 20178-20184.
56. M. Hamad, DOI: http://hdl.handle.net/20.500.11937/86652, Curtin University; http://hdl.handle.net/20.500.11937/86652, 2021.
57. P. B. Hirsch, A. Howie, R. B. Nicholson, D. W. Pashley and M. J. Whelan, *Electron Microscopy of Thin Films*, Butterworths, London 1965.
58. C. F. Macrae, I. J. Bruno, J. A. Chisholm, P. R. Edgington, P. McCabe, E. Pidcock, L. Rodriguez-Monge, R. Taylor, J. van de Streek and P. A. Wood, *Journal of Applied Crystallography*, 2008, **41**, 466-470.
59. G. M. Parkinson, M. J. Goringe, S. Ramdas, J. O. Williams and J. M. Thomas, *Journal of the Chemical Society, Chemical Communications*, 1978, DOI: 10.1039/C39780000134, 134-135.
60. S. Ramdas, G. M. Parkinson, J. M. Thomas, C. M. Gramaccioli, G. Filippini, M. Simonetta and M. J. Goringe, *Nature*, 1980, **284**, 153-154.
61. C. M. Gramaccioli, G. Filippini, M. Simonetta, S. Ramdas, G. M. Parkinson and J. M. Thomas, *Journal of the Chemical Society, Faraday Transactions 2: Molecular and Chemical Physics*, 1980, **76**, 1336-1346.
62. J. Bernstein, J. D. Dunitz and A. Gavezzotti, *Crystal Growth & Design*, 2008, **8**, 2011-2018.
63. B. Marciniak and V. Pavlyuk, *Molecular Crystals and Liquid Crystals*, 2002, **373**, 237-250.
64. D. E. Williams, *The Journal of Chemical Physics*, 1967, **47**, 4680-4684.